Effect of Cu Substitution on Magnetic and DC Electrical Resistivity Properties of Ni-Zn Nano Ferrites

K. Chandramouli
Andhra University College of Engineering
P. Anantha Rao
Andhra University College of Engineering
B. Suryanarayana
Andhra University College of Engineering
Vemuri Raghavendra
Aditya College of Engineering and Technology
D. Parajuli
Andhra University
Paulos Taddesse
Arba Minch University
Tulu Wegayehu Mammo
Aksum University
M. K. Raju
WISTM Engineering College
Dr. Murali Nandigam (muraliphdau@gmail.com)
Andhra University College of Engineering https://orcid.org/0000-0002-8272-2802

Research Article

Keywords: Cu substituted Ni-Zn ferrite, XRD, FTIR, Magnetic, Electrical properties

Posted Date: February 23rd, 2021

DOI: https://doi.org/10.21203/rs.3.rs-251417/v1

Effect of Cu substitution on magnetic and DC electrical resistivity properties of Ni-Zn nano ferrites

K. Chandramouli[1], P. Anantha Rao[1], B. Suryanarayana[1], Vemuri Raghavendra[2], D. Parajuli[3], Paulos Taddesse[4], Tulu Wegayehu Mammo[5], M. K. Raju[6], *N. Murali[1]

[1]Department of Engineering Physics, AUCE (A), Andhra University, Visakhapatnam

[2]Department of Physics, Aditya College of Engineering and Technology, Surampalem

[3]Department of Physics, AUCST, Andhra University, Visakhapatnam

[4]Department of Physics, College of Natural Science, Arba Minch University, Ethiopia

[5]Department of Physics, CNCS, Aksum University, Axum, Ethiopia

[6]Department Physics, WISTM Engineering College, Pinagadi, Visakhapatnam

*Corresponding author email:muraliphdau@gmail.com

Abstract: Cu substituted $Ni_{0.5}Zn_{0.5-x}Cu_xFe_2O_4$ (x = 0, 0.1, 0.2, 0.3 and 0.4) samples is synthesized using the sol-gel auto-combustion process. X-ray diffraction shows its cubic spinel structure. The lattice constant decreases as the Cu content increases. The sizes of the crystallites are also decreasing in the range of 42.68 nm to 21.75 nm. The wavenumbers of tetrahedral and octahedral sites sighted in the FTIR spectra are similar to that of the precursor. The increment in the copper content increases the DC conductivity. The electrical resistivity decrease with increase in the temperature, i.e. it has a negative temperature coefficient with resistance similar to semiconductors. The remnant ratios R obtained from VSM show their isotropic nature forming single domain ferrimagnetic particles. The resultant material is widely significant, as indicated by its result.

Keywords: Cu substituted Ni-Zn ferrite, XRD, FTIR, Magnetic, Electrical properties.

INTRODUCTION

These spinel nanomaterials or ferrites with cations in their tetrahedral and octahedral sites are used as soft magnetic materials in everyday life [1-3]. Changing their internal with doping can make them applicable in more advanced devices. Most of the spinel ferrite materials have $M^{2+}Fe_2^{3+}O_4^{2-}$ the type of structure, where, M is Transitional Metal Cation. M is on the tetrahedral site and Fe on the octahedral site of the spinel. This soft magnetic ferrite's high resistivity and low power loss made them be used in multilayered chip inductors, microwave absorption materials, information storage system, transformer core, computer circuitry and electronic communication. Among them, Ni-Zn ferrite is one that is highly stable at a higher frequency. Ni–Cu–Zn ferrites are used in Multilayer Chip Inductors (MLCI)

and Surface Mounting Devices (SMDs). As a result, they are utilized in cellular phones, video cameras, notebook computers, personal wireless communication systems, etc. their properties can be changed by varying the concentration of Cu^{2+} and found to be more applicable in inductive devices like transformers. [4, 5]. The ferrites prepared at low temperature are used in multilayer power inductors and transformers.

The purpose of this study is to a sol-gel auto-combustion method for the synthesis of the samples $Ni_{0.5}Zn_{0.5-x}Cu_xFe_2O_4$ ($0.0 \leq x \leq 0.4$) nanoparticles and investigates the influence of chemical composition, DC electrical resistivity and magnetic properties. Ni–Cu–Zn ferrites have been studied for different electrical and magnetic applications [6]. Albeit high dielectric constants, i.e. electrical properties have been reported for these ferrites, the correspondingly high dielectric loss, especially at high operating frequencies, hampers their application in reality [7]. In this work, $Ni_{0.5}Zn_{0.5-x}Cu_xFe_2O_4$ ($0.0 \leq x \leq 0.4$) nanoparticles with different compositions of Ni: Zn: Cu are prepared to DC electrical and magnetic properties of synthesized nanomaterials. Zn^{2+} is one of the most stable cations in Ni-Zn-Cu ferrites. Therefore, Zn^{2+} is supposed to play an essential role in stabilizing the crystal lattice and optimising the resulting nanoparticles' properties.

In this work, Cu substituted nickel-zinc ferrites are prepared by sol-gel auto combustion method, and their different properties are studied using XRD, FESEM, FTIR, DC resistivity, VSM etc.

EXPERIMENTAL TECHNIQUES

Copper Substituted Nickel-Zinc nanoparticles are prepared by the sol-gel auto-combustion method. 99.99% pure Nickel nitrate, Copper nitrate, Zinc nitrate, Iron nitrate and citric acid monohydrate with the molecular formula (Ni $(NO_3)_2 \cdot 6H_2O$), (Zn $(NO_3)_2 \cdot 6H_2O$), Cu $(No_3)_3 \cdot H_2O$, (Fe $(NO_3)_3 \cdot 9H_2O$) and ($C_6H_8O_7.H_2O$) respectively, as the starting materials. They are mixed in such a ratio that $Ni_{0.5-x}Cu_xZn_{0.5}Fe_2O_4$ (x = 0.0, 0.05, 0.1, 0.15 and 0.2) samples are prepared. These metal nitrates and citric acid were mixed in a molar ratio of 1:1 and were dissolved in the distilled water to get a clear solution. The solution was made neutral by adding liquid ammonia. The solution was then stirred in magnetic stirrer maintained at 100 ^oC for 4 h, decanted and dried at normal temperature for 40 h. The flakes thus obtained were combusted and converted into a powder. The powder was sintered in a muffle furnace at 800 °C for 4 h at 5^o/min.

We used Rigaku X-ray diffractometer (Rigaku Miniflex II) incorporated with CuKα radiation of wavelength = 1.5406 Å for the structural property, TESCAN, MIRA II LMH

SEM with attached Inca Oxford EDX for textural and compositional images, FT-IR analysis for the detection of functional group, EZ VSM model for the magnetic at room temperature. Few drops of polyvinyl alcohol were mixed with the powder for shaping them into disc-like pallets after pressing them in a die under the hydraulic press of 5 tons. The pallets were then made as an electrode by sintering them in 800^{o}C in a muffle furnace and polishing their flat sides with gold. Their conductivity was checked by the two-probe DC resistivity method.

3. RESULTS AND DISCUSSIONS

3.1 XRD Studies

The XRD plots of different $Ni_{0.5}Zn_{0.5-x}Cu_xFe_2O_4$ (x = 0, 0.1, 0.2, 0.3 and 0.4) samples are shown in Figure 1. The structure of the sample is found to be cubic spinel structure according to the JCPDS card No.48-0489. The lattice constant 'a' is determined with the following relation [8].

$$\mathbf{a = d_{hkl}\sqrt{h^2 + k^2 + l^2}}$$

where d_{hkl} is interplaner spacing for given hkl planes and is calculated by Bragg's law, the highest intensity (311) peak indicates the crystallites appropriate orientation to measure its degree of crystalline nature to find the average crystallite size of all samples [9]. Debye-Scherer's formula gives the average size of the crystallite size [10].

$$D_{311} = \frac{0.9\lambda}{\beta cos\theta}$$

where, D_{311}, λ, β and θ are volume-averaged crystallite size, the wavelength of X-ray (1.5406Å), full width at half maximum of (311) peak and diffraction angle respectively.

The crystallite size and lattice parameters of the composition $Ni_{0.5}Zn_{0.5-x}Cu_xFe_2O_4$ (x = 0.0, 0.1, 0.2, 0.3 and 0.4) is listed in Table 1. The crystallite size first decreases from 42.68 nm to 21.75 nm (for x=0.0 to 0.0.4). In contrast, the lattice parameter decreases with increases in the Cu^{2+} ions concentration. This is due to the greater ionic radius of Zn^{2+} ions (0.74 Å) [12] as compared to Cu^{2+} (0.73 Å) [13] thereby expanding the unit cell or decreasing lattice constant [14] as shown in figure 3. The obtained value of the lattice parameter of base (x = 0) sample is 8.3894 Å to 8.3499 Å. It is well-matched with the value reported in the literature [33]. The lattice compression may also be due to the partial oxidation of Zn^{2+} to Zn^{3+}, Cu^{2+} to Cu^{3+}. The zinc loss and gain are usually credited to the surface, forming a common boundary structure between surfaces with a more volume fraction. The variation of lattice constant is more significant in a smaller size of the nanoparticle.

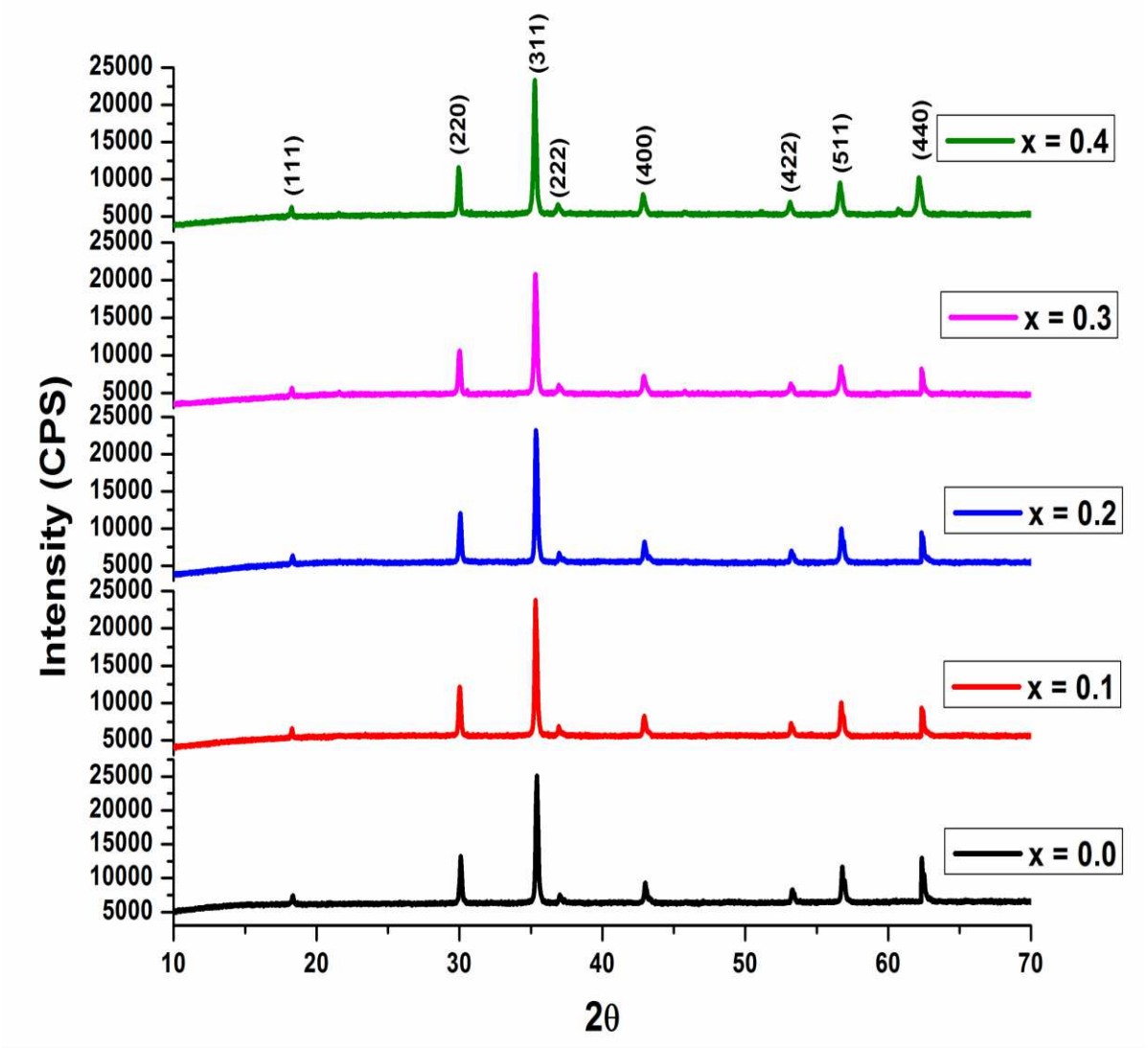

Figure 1: X-ray diffraction patterns of $Ni_{0.5}Zn_{0.5-x}Cu_xFe_2O_4$ (x=0.0, 0.01, 0.2, 0.3 and 0.4) ferrites

TABLE 1: Lattice parameters of $Ni_{0.5}Zn_{0.5-x}Cu_xFe_2O_4$ (x=0.0, 0.01, 0.2, 0.3 and 0.4) ferrites

Concentration (x)	***a* (Å)**	**Crystallite (nm)**	**Space Group**
0.0	8.3894	42.68	*Fd-3m*
0.1	8.3876	29.35	*Fd-3m*
0.2	8.3808	25.51	*Fd-3m*
0.3	8.3551	23.63	*Fd-3m*
0.4	8.3499	21.75	*Fd-3m*

From Scherer's formula, the diffraction peak width (β) is inversely proportional to the crystallite size. The increase in the lattice parameter expands the volume of the unit cell accordingly. Sintering decreases the lattice defects and involved strain but facilitates the crystals' coalition increasing in particle size.

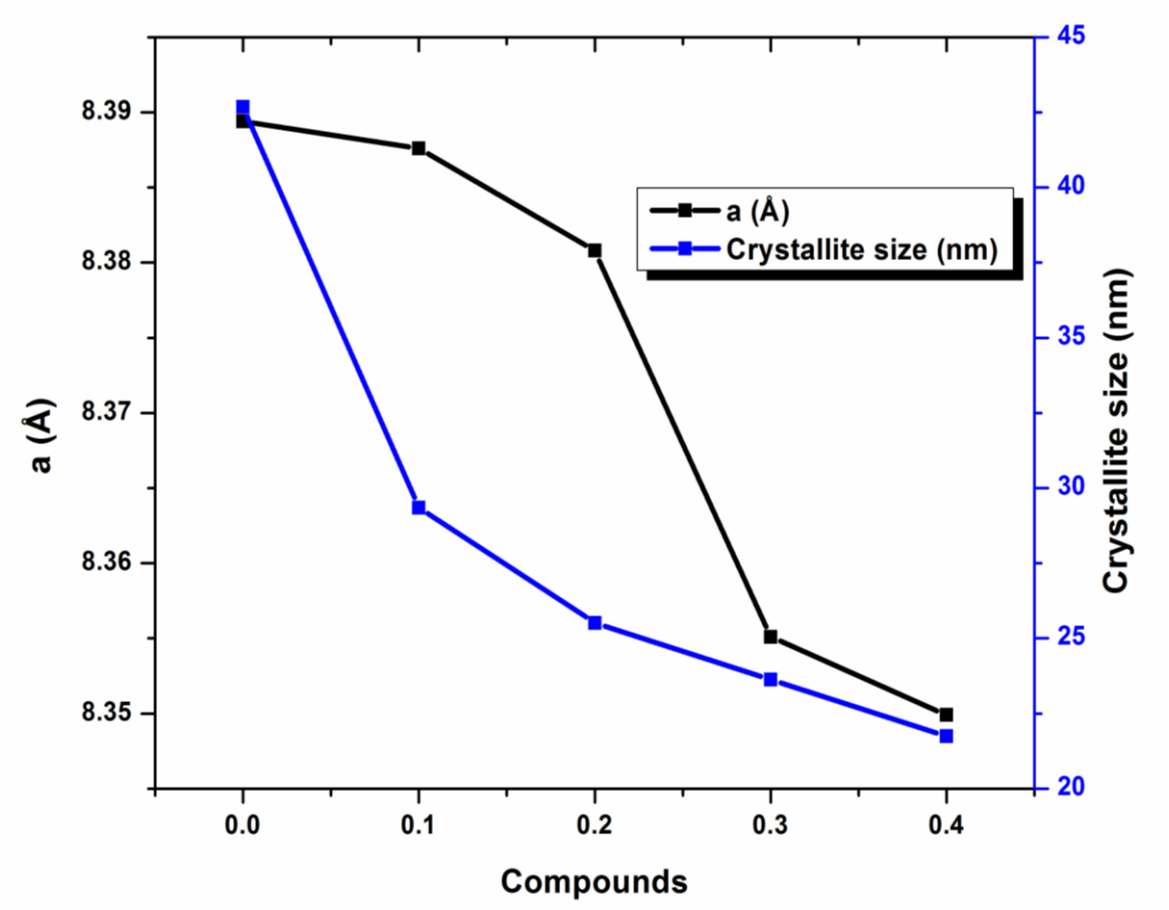

Figure 2: Variation of lattice constant and crystallite size of $Ni_{0.5}Zn_{0.5-x}Cu_xFe_2O_4$ (x=0.0, 0.01, 0.2, 0.3 and 0.4) ferrites

3.2 Field-Effect Scanning Electron Microscope (FESEM) with EDS

The FESEM images from Figure 3 show that the nickel, copper and zinc are not miscible, and the average size of the grain ranges from 0.2 to 0.4μm. The grains sizes are nearly equal [15]. The microstructure images like grain size, pores, inclusions, grain boundaries, particle size, homogeneity, defects etc. can be obtained with the help of Electron microscope. The smaller grain size with low porosity controls excessive spin-wave production, which is essential for microwave devices. Similarly, the large grain size supports the mobility of the domain wall, resulting in high permeability with low coercive value. Also, the eddy current loses is checked by the grain boundaries acting as current barriers. The elemental composition of O, Fe, Ni, Zn is seen on the Ni-Zn ferrites with EDS's help, as shown in Figure 4.

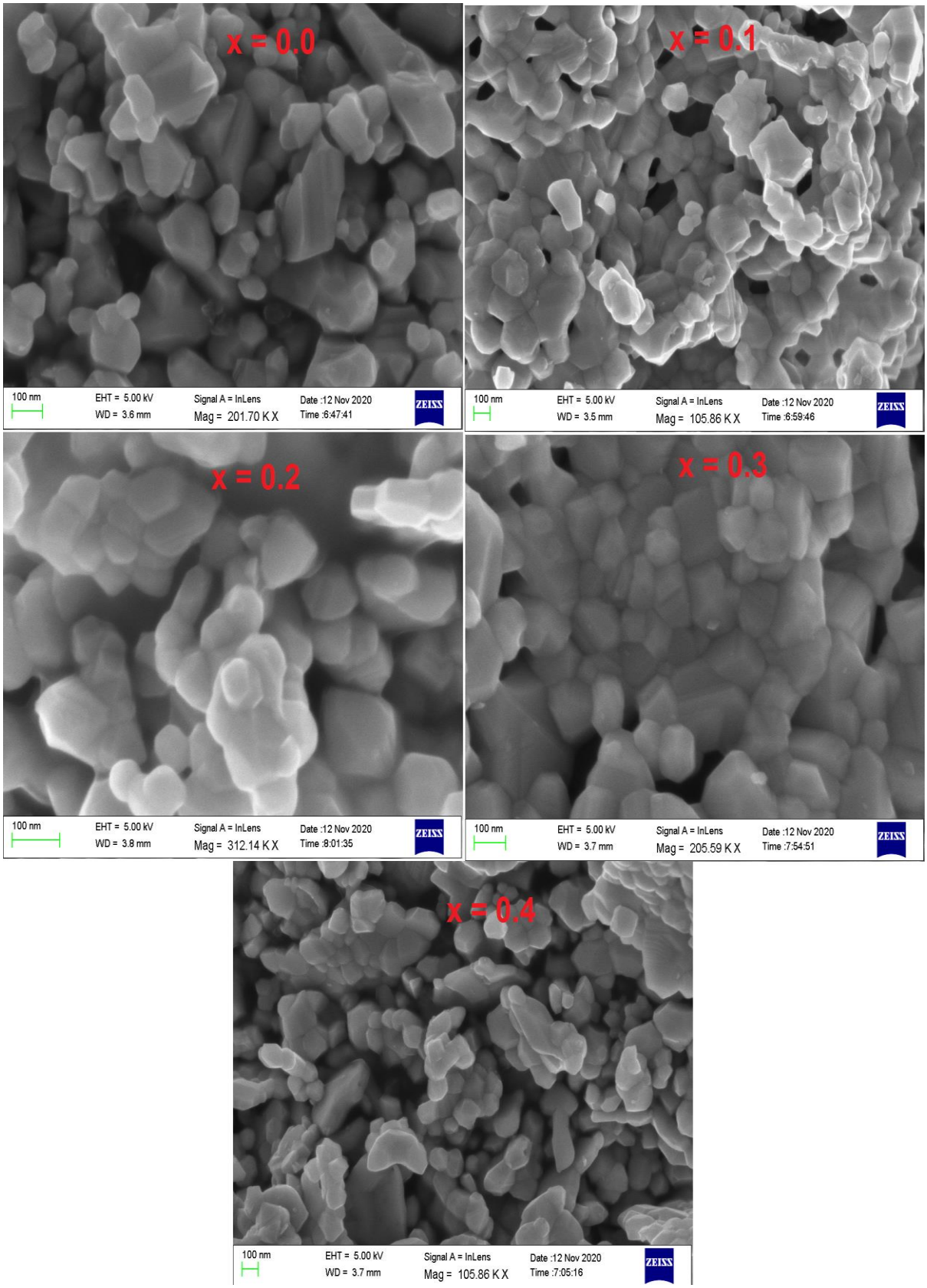

Figure 3: FESEM images for of $Ni_{0.5-x}Cu_xZn_{0.5}Fe_2O_4$ (x = 0.0, 0.05, 0.1, 0.15 and 0.2) ferrites

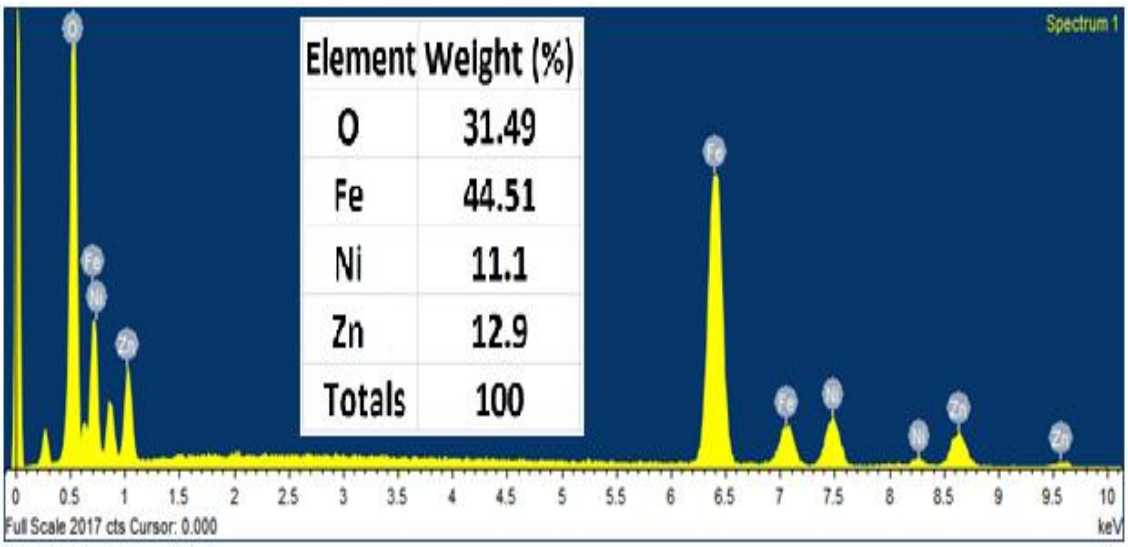

Figure 4: EDS counts and elemental weight for $Ni_{0.5}Zn_{0.5}Fe_2O_4$ ferrite NPs

3.3 Fourier Transformed Infrared (FTIR) Spectroscopy studies

The FTIR spectroscopy helps determine the different functional groups for their wavenumbers or how the absorption occurs. Our sample's FTIR spectra within the range of 400-1200 cm^{-1} are shown in figure 5. The spinel or inverse spinel ferrite can show four IR active regions or high intensity or non-zero dipole moment regions in the vibrational spectra. First, three of them are the resultant of tetrahedral and octahedral compounds, and the forth is due to the lattice vibration of the tetrahedral cation. The two absorption bands at wavenumbers 580.4 to 598.84 cm^{-1} and 402.1 to 405.35 cm^{-1} seen as two depressions in figure 6 and values listed in Table 2 are the two respective characteristics bands of each spinel ferrite. The bond length between Fe^{3+} and O^{2-} is varied for the sample composition, resulting in the deviation in the peak position of v_1 and v_2 towards high-frequency region [16].

Table 2: Absorption bands of $Ni_{0.5}Zn_{0.5-x}Cu_xFe_2O_4$ (x=0.0, 0.01, 0.2, 0.3 and 0.4) ferrites

Concentration (x)	Tetrahedral $\upsilon_1(cm^{-1})$	Octahedral $\upsilon_2(cm^{-1})$
0.0	580.40	402.1
0.1	582.85	403.48
0.2	585.92	404.46
0.3	591.05	407.85
0.4	598.84	405.35

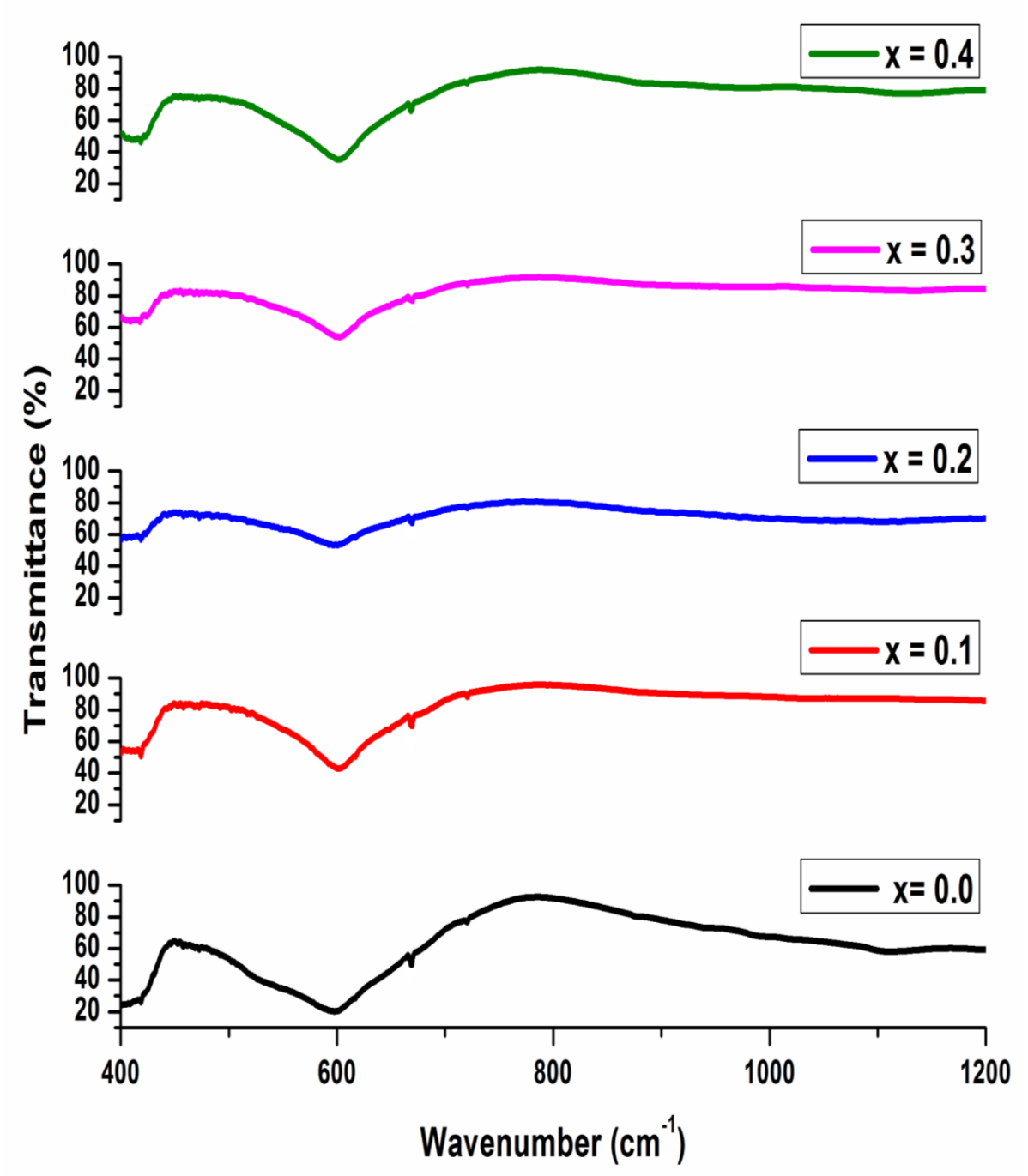

Figure 5: Infrared spectra of of $Ni_{0.5}Zn_{0.5-x}Cu_xFe_2O_4$ (x=0.0, 0.01, 0.2, 0.3 and 0.4) ferrites

3.4 Magnetic properties

Ferrites have antimagnetic moments with unequal magnitudes. As a result, they have a large value of spontaneous magnetization. The exchange integral, depending on interatomic distance, is negative for ferrite. This indirect exchange interaction through oxygen ions limits the easy flow of electron. So, ferrites have high resistivity [17].

The magnetic properties like saturation permeability, coercivity, susceptibility, Curie temperature etc. of ferrites depend on the concentration of metal ions

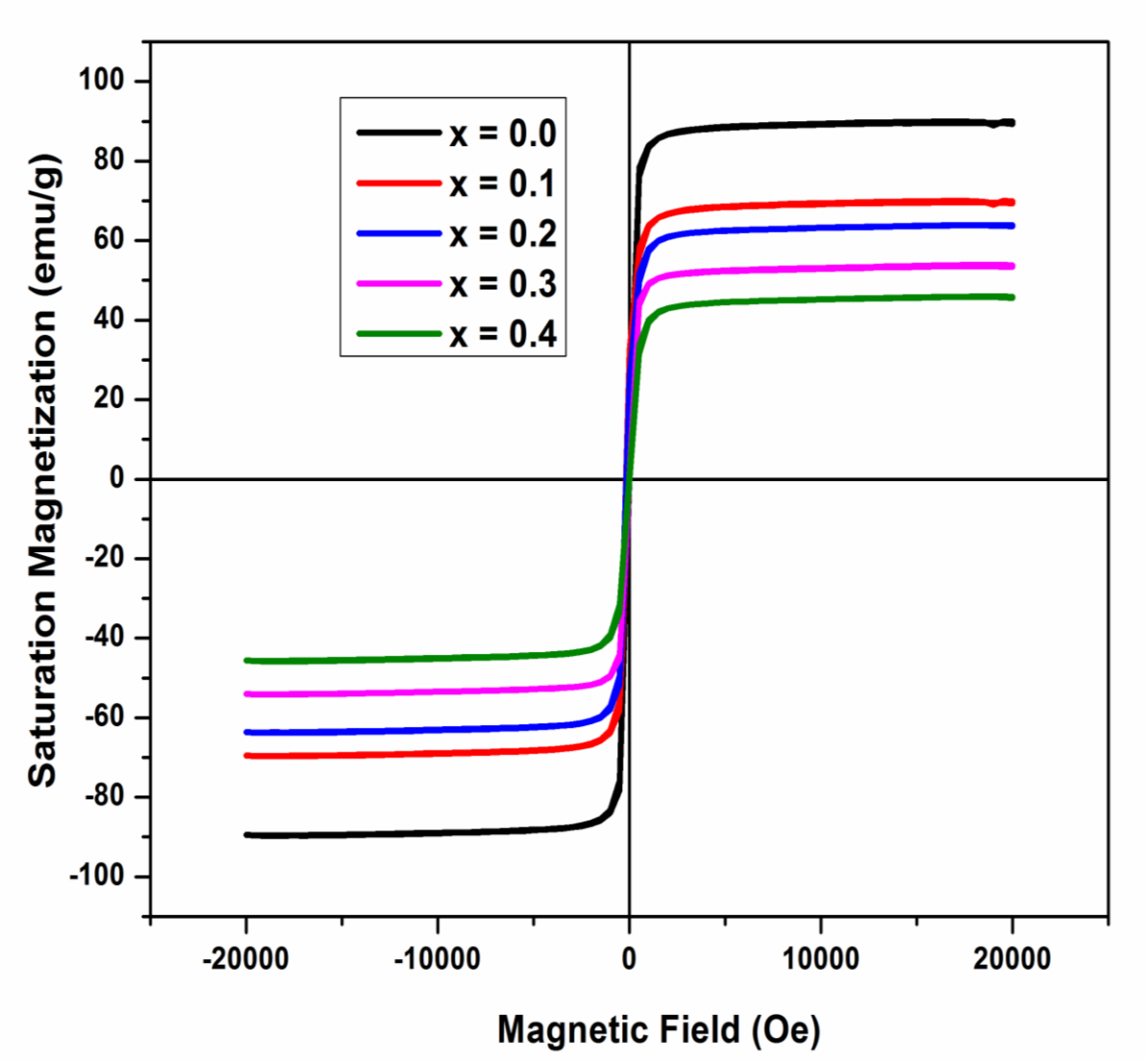

Figure 6: Hysteresis curve of $Ni_{0.5}Zn_{0.5-x}Cu_xFe_2O_4$ (x=0.0, 0.01, 0.2, 0.3 and 0.4) ferrites

on both the octahedral and tetrahedral sites. The hysteresis loop shapes, resistivity, ac conductivity, and dielectric constant depend on the ferrite structure. So, these properties are more sensitive to the structure. These properties can be changed by adding external magnetic or non-magnetic metal ions. The hysteresis curves of our respective samples are as shown in figure 6. Figure 7 shows the values of coercivity (Hc), saturation magnetization (Ms) etc. that are important for their magnetic properties. The values of Ms and Hc are listed in Table 3 [18].

From table 3, Ms values are decreases in decreasing Cu^{2+} concentration. On adding copper ions to Nickel-Zinc mixture, they exchange few magnetic ions Fe^{3+} and Ni^{2+} in B- site increases AB interaction that interrupts the antiparallel spin at B site resulting from the increase in total magnetization [19]. A similar phenomenon occurs on the A site. According to Weiss Molecular field theory, the A-B and B-A interaction dominate the A-A and B-B interaction resulting in the hysteresis loop [20-21].

Table 3: Ms and Hc of $Ni_{0.5}Zn_{0.5-x}Cu_xFe_2O_4$ (x=0.0, 0.01, 0.2, 0.3 and 0.4) ferrites

Concentration (x)	M_s (emu/g)	H_c (Oe)
0.0	89.93	45.36
0.1	69.93	90.48
0.2	63.82	110.87
0.3	53.75	156.74
0.4	45.82	245.86

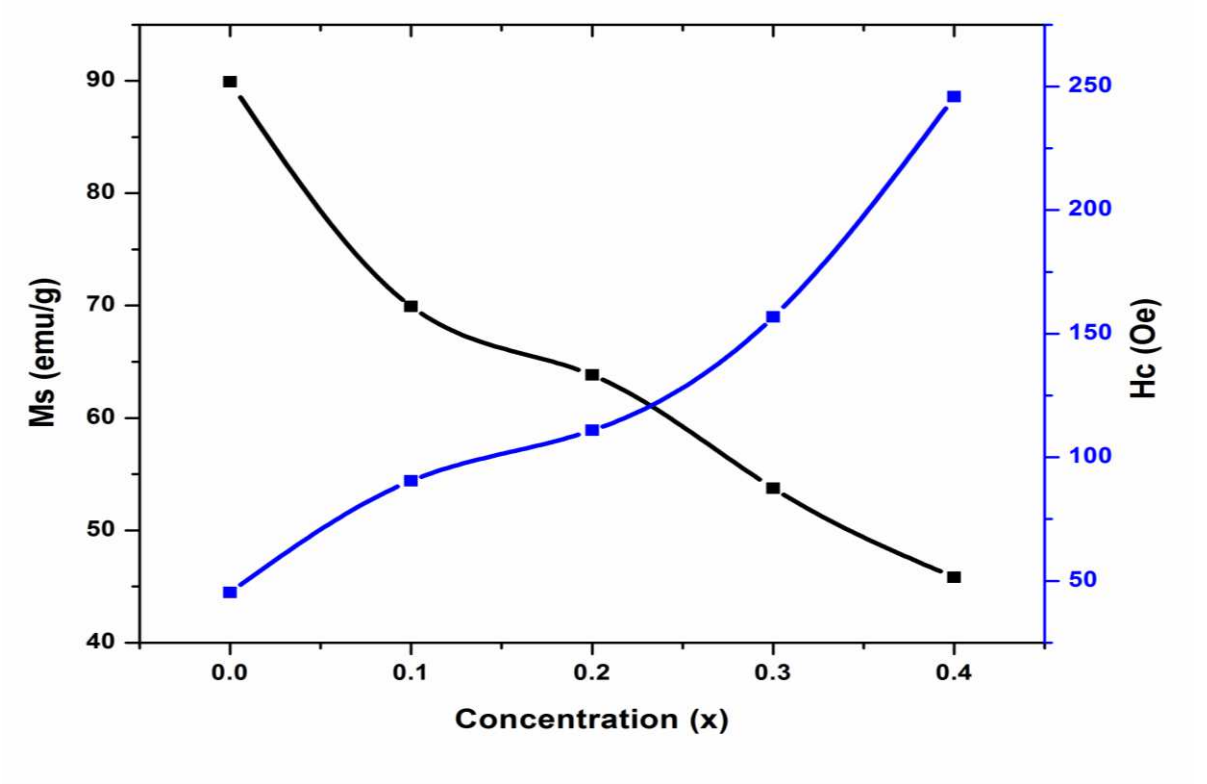

Figure 7: Variation of saturation magnetization and coercivity of $Ni_{0.5}Zn_{0.5-x}Cu_xFe_2O_4$ (x=0.0, 0.01, 0.2, 0.3 and 0.4) ferrites

3.5 DC Electrical Resistivity

The DC resistivities of $Ni_{0.5}Zn_{0.5-x}Cu_xFe_2O_4$ (x=0.0, 0.01, 0.2, 0.3 and 0.4) ferrites nanoparticles initially decreases rapidly, then steadily and then continue with the further increase in Cu concentration. The plot of DC resistivity vs temperature for the Cu substituted Ni-Zn is shown in figure 8. A graph between log ρ and 1000/T is a straight line. It shows that the resistivity decreases with increase in temperature showing semiconducting behaviour. The slope of the line gives the activation energies of the ferrite samples. The dc resistivity data are used in Arrhenius to find the activation energy of the thermally activated hopping of charge carriers [22].

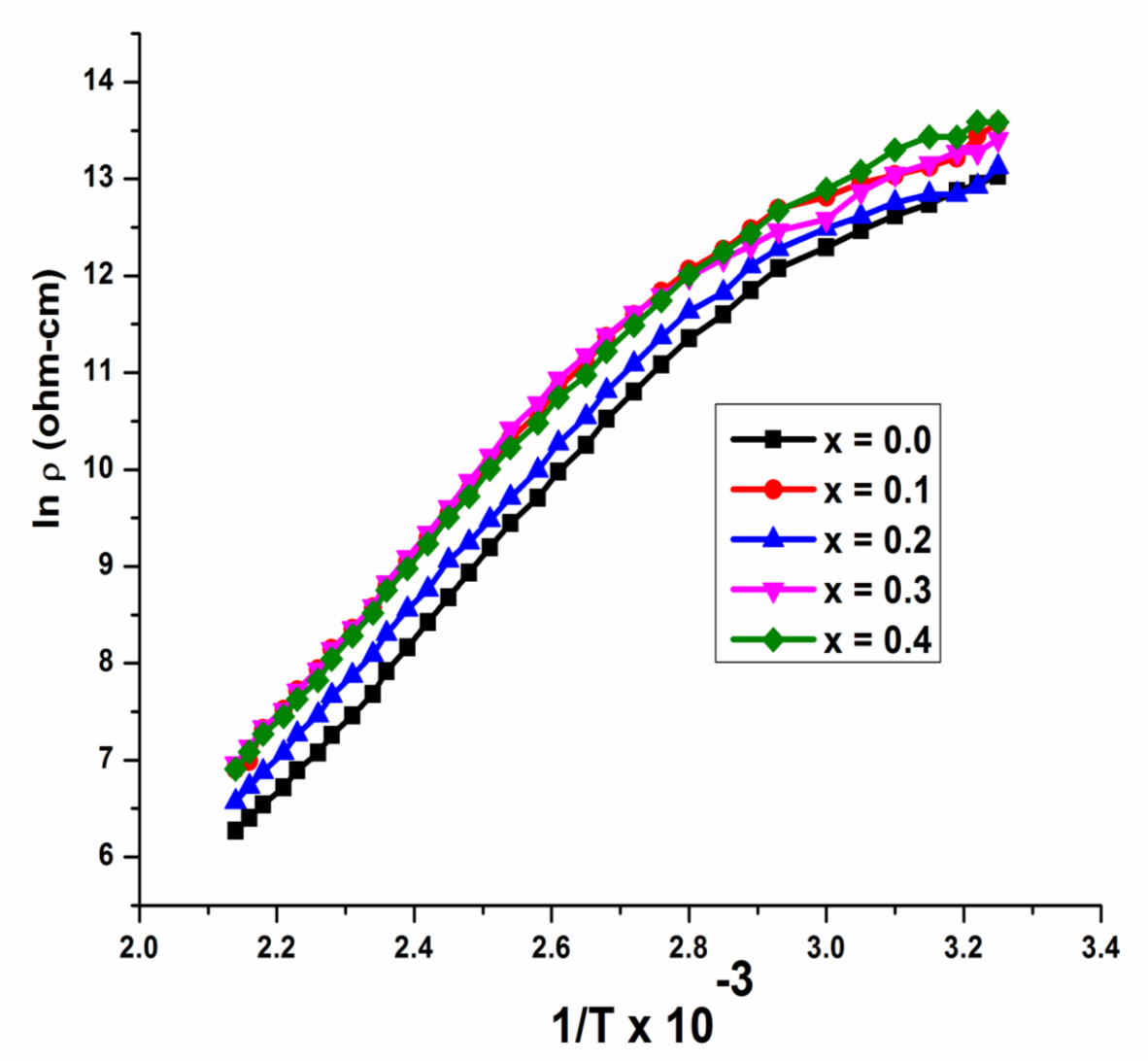

Figure 8: Temperature dependence of DC resistivity of $Ni_{0.5}Zn_{0.5-x}Cu_xFe_2O_4$ (x=0.0, 0.01, 0.2, 0.3 and 0.4) ferrites

The Arrhenius relation is,

$$\rho = \rho_o e^{-\left(\frac{\Delta E}{KT}\right)}$$

where ρ is the dc electrical resistivity at temperature T, ρ_o is the pre-exponential factor, ΔE is the activation energy, K is the Boltzmann constant and T is the absolute temperature. The calculated values of activation energies of the Cu doped Ni-Zn ferrite nanoparticles ferrite samples are shown in Figure 9. Verwey and de Boer hopping mechanism helps to interpret the resistivity variation for the Cu doped Ni-Zn ferrite nanoparticles. Electron hopping occurs between ions of the same element located at different valance states and the two sites. During sintering of the ferrites, the divalent and trivalent iron ions can be produced and exist in octahedral sites that help in electrical conduction through $Fe^{2+} \Leftrightarrow Fe^{3+}$ hopping mechanism. If the ferrite's sintering temperature is higher, more Fe^{2+} ions are produced, thereby accelerating the hopping process. The hopping process is possible in $Zn^{2+} \Leftrightarrow Zn^{3+}$ and $Cu^{3+} \Leftrightarrow Cu^{2+}$ existing together in a system [23].

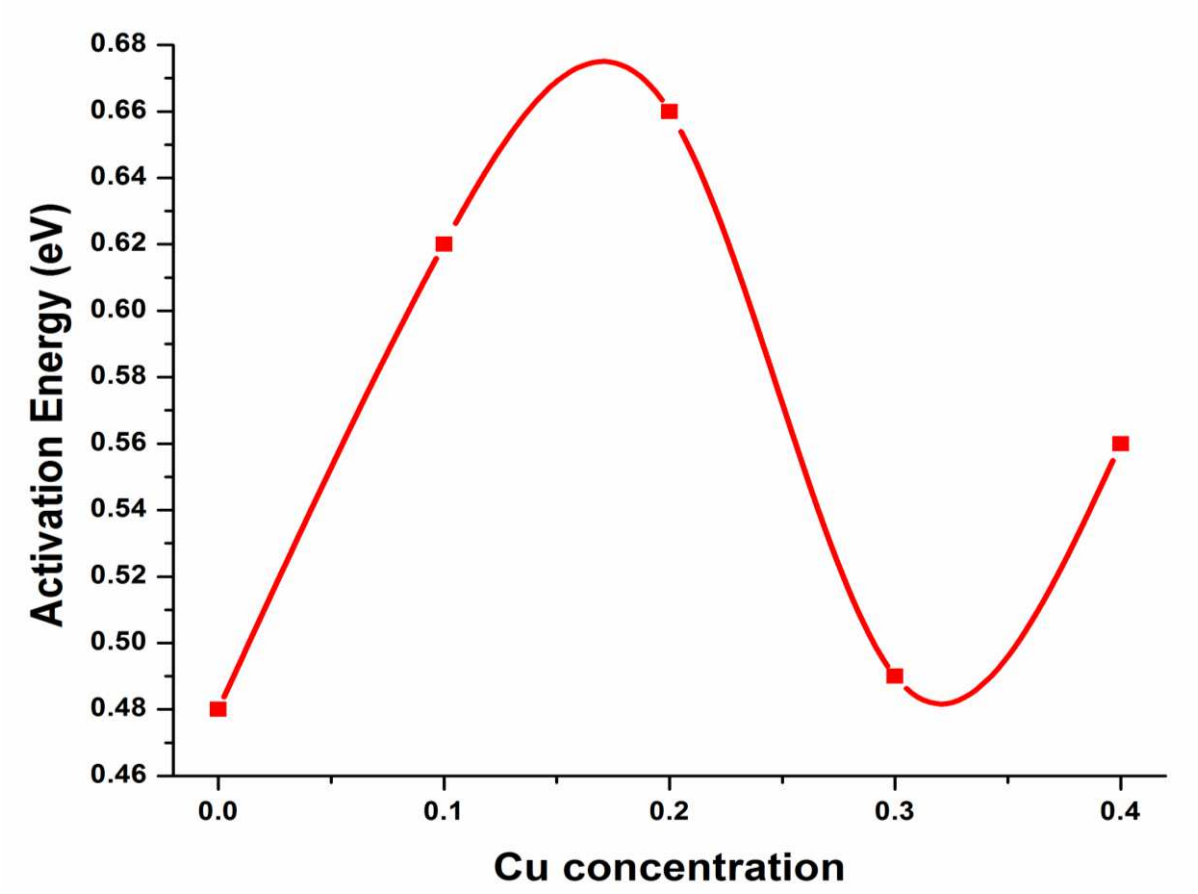

Figure 9: Activation energies of the $Ni_{0.5}Zn_{0.5-x}Cu_xFe_2O_4$ (x=0.0, 0.01, 0.2, 0.3 and 0.4) ferrites

About the above calculation as in figure 8, the activation energies are found to be in the order of 0.42 to 0.51 eV which is for the $Fe^{2+} \Leftrightarrow Fe^{3+}$ electron hopping mechanism. It indicates that the major conduction mechanism is $Fe^{2+} \Leftrightarrow Fe^{3+}$ process. Besides, the conduction processes such as $Fe^{2+} + Zn^{3+} \Leftrightarrow Fe^{3+} + Zn^{2+}$ ions require relatively more energy for electron hopping so that the energy required could be slightly more than 0.42 eV. The temperature-dependent resistivity and associated activation energies indicate the compositional dependence of resistivity [24].

4. CONCLUSIONS

Sol-gel auto-combustion method is utilized to fabricate nanocrystalline $Ni_{0.5}Zn_{0.5-x}Cu_xFe_2O_4$ (x=0.0, 0.01, 0.2, 0.3 and 0.4) ferrite NPs. The structure of the ferrite shown by the X-ray diffraction is single phase cubic spinel. The decreasing crystallite size values increasing the Cu concentration. In comparison, the lattice parameter decreases with the increases in Cu^{2+} ions concentration. This is due to the greater ionic radius of Zn^{2+} ions (0.74 Å) than Cu^{2+} (0.73 Å), thereby expanding the unit cell or decreasing lattice constant. FESEM reveals microstructural growth along with heat action. The FTIR spectrum exhibits a prominent attribute of ferrite microstructure and a major impact on ingredients' mixture. The magnetic measurements show that magnetization reduces and coercivity enhances. DC resistivity is decreasing with an increase in the content of copper due to its highly conducting property. The electrical resistivity decrease with increase in the temperature, i.e. it has a negative temperature coefficient with resistance similar to semiconductors. The temperature-dependent resistivity and associated activation energies indicate the compositional dependence of resistivity.

REFERENCES

[1] Yu S, Wu G, Gu X, Wang J, Wang Y, Gao H, et al. Colloids Surf, 103 (2013) 15–22.

[2] Tejabhiram Y, Pradeep R, Helen AT, Gopalakrishnan C, Ramasamy C. Mater Res Bull 2014;60:778–82.

[3] Jha DK, Shameem M, Patel AB, Kostka A, Schneider P, Deb AEP. Mater Lett 2013;95:186–9.

[4] Kenouche S, Larionova J, Bezzi N, Guari Y, Bertin N, Zanca M, et al. Powder Technol 2014;255:60–5.

[5] A. Ramakrishna, N. Murali, Tulu Wegayehu Mammo, K. Samatha, V. Veeraiah, Phys. B: Condens. Matter 534 (2018)134-140.

[6] Min Ji Hyun, Woo Mi-Kyung, Yoon Ha Young, Jang Jin Woo, Wu Jun Hua, Lim Chae-Seung, et al. Anal Biochem 2014;447:114–8.

[7] Drmota A, Koselj J, Drofenik M, Znidarsic A. J Magn Magn Mater 2012;324:1225–9.

[8] B.D. Cullity, (1956), Elements of X-ray diffraction, Addison Wesley Publication reading, M.A.

[9] Costa ACFM, Leite AMD, Ferreira HS, Kiminami RHGA, Cavac S, Gama L. J Eur Ceram Soc 2008;28:2033–7.

[10] C. Nlebedim, K.W. Dennis, R.W. McCallum, D.C. Jiles, J. Appl. Phys. 115 (2014) 17A519.

[11] James V, Rao PP, Sameera S, Divya S. Ceram Int 2014;40(Issue 1 Part B):2229–35.

[12] Netto CGCM, Toma HE, Andrade LH. J Mol Catal B Enzym 2013;85–86:71–92.

[13] Guo F, Fang Z, Xu CC, Smith Jr RL. Prog Energy Combust Sci, Oxford, Inglaterra, GB 2012;38 (5):672–90.

[14] Jing H, Wang X, Liu Y, Wang A. Chin J Catal 2015;36(2):244–51.

[15] Akhtar MN, Khan MA, Ahmad M, Nazir MS, Imran M, Ali A, et al. J Magn Magn Mater 2017;421:260–8.

[16] Ambursa MM, Ali TH, Lee HV, Sudarsanam P, Bhargava SK, Hamid SBA. Fuel 2016;180:767–76.

[17] Li Y, Zhang C, Liu Y, Tang S, Chen G, Zhang R, et al. Fuel 2017;189:23–31.

[18] Jain SR, Adiga KC, Verneker VP. Combust Flame 1981;40:71–9.

[19] Klung H, Alexander L. New York: Wiley; 1962.

[20] N. Murali, S. Margarette, G.P. Kumar, B. Sailaja, S.Y. Mulushoa, P. Himakar, B.K. Bab, V. Veeraiah, Phys. B Condens. Matter, 522 (2017) 1-6

[21] Reed JS. New York: John Wiley & Sons; 1996.

[22] Kumar S, Kumar P, Singh V, Kumar Mandal U, Kumar Kotnala R. J Magn Magn Mater 2015;379:50–7.

[23] Andreev VG, Menshova SB, Klimov AN, Vergazov RM. J Magn Magn Mater 2015;393:569–73.

[24] Batoo KM, Ansari MS. Nanoscale Res Lett 2012;7(1):1–14.

Figures

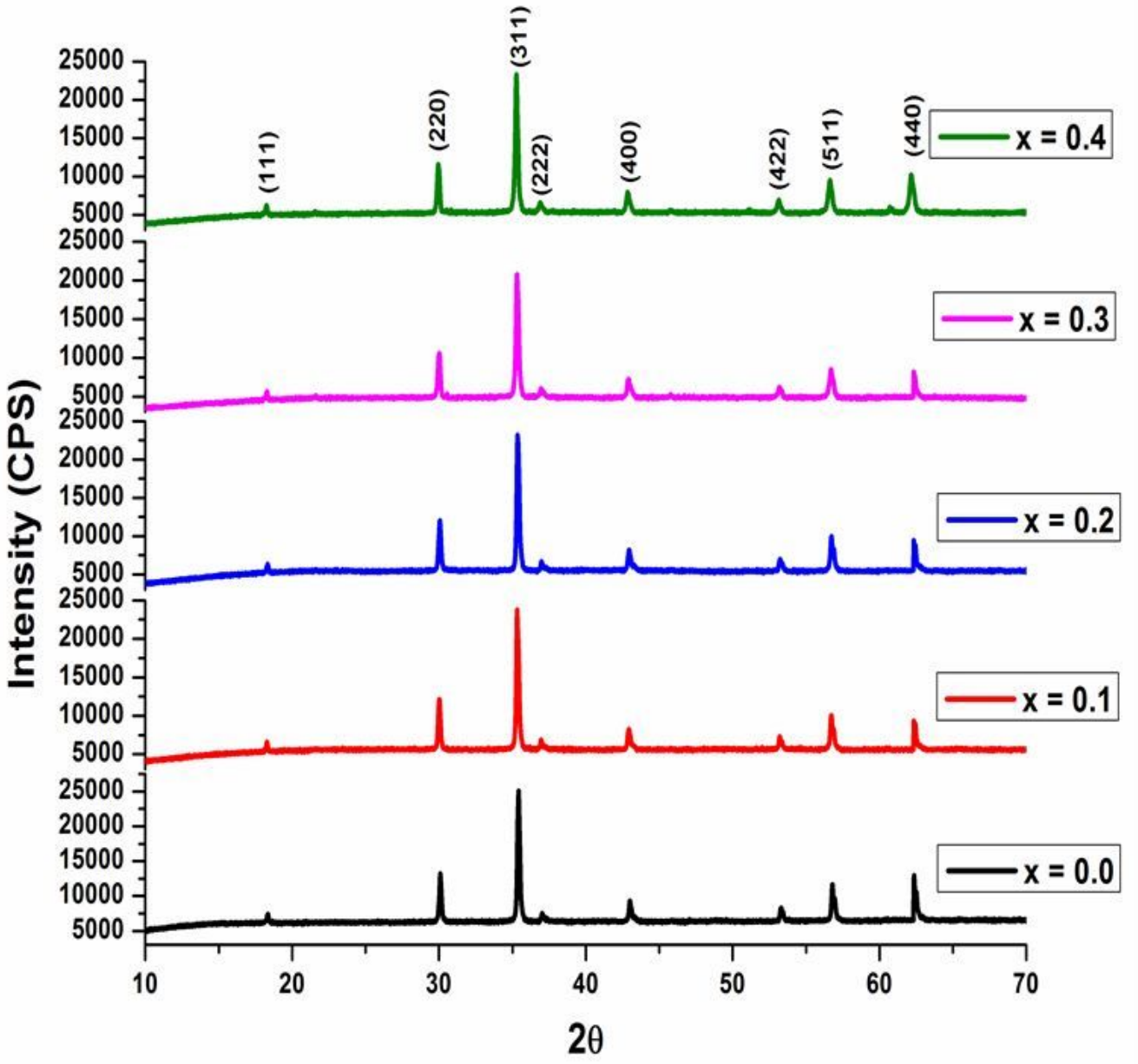

Figure 1

X-ray diffraction patterns of Ni0.5Zn0.5-xCuxFe2O4 (x=0.0, 0.01, 0.2, 0.3 and 0.4) ferrites

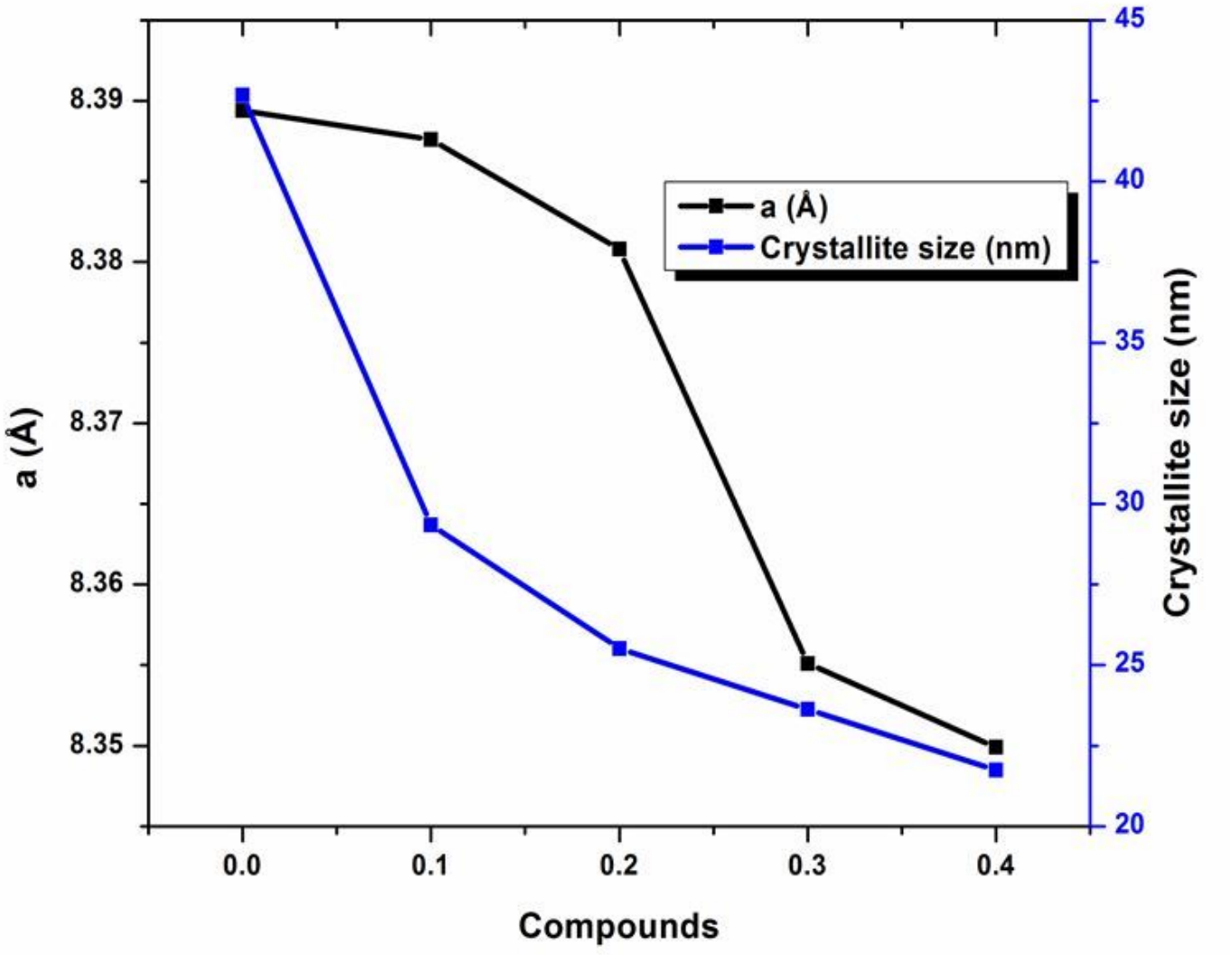

Figure 2

Variation of lattice constant and crystallite size of Ni0.5Zn0.5-xCuxFe2O4 (x=0.0, 0.01, 0.2, 0.3 and 0.4) ferrites

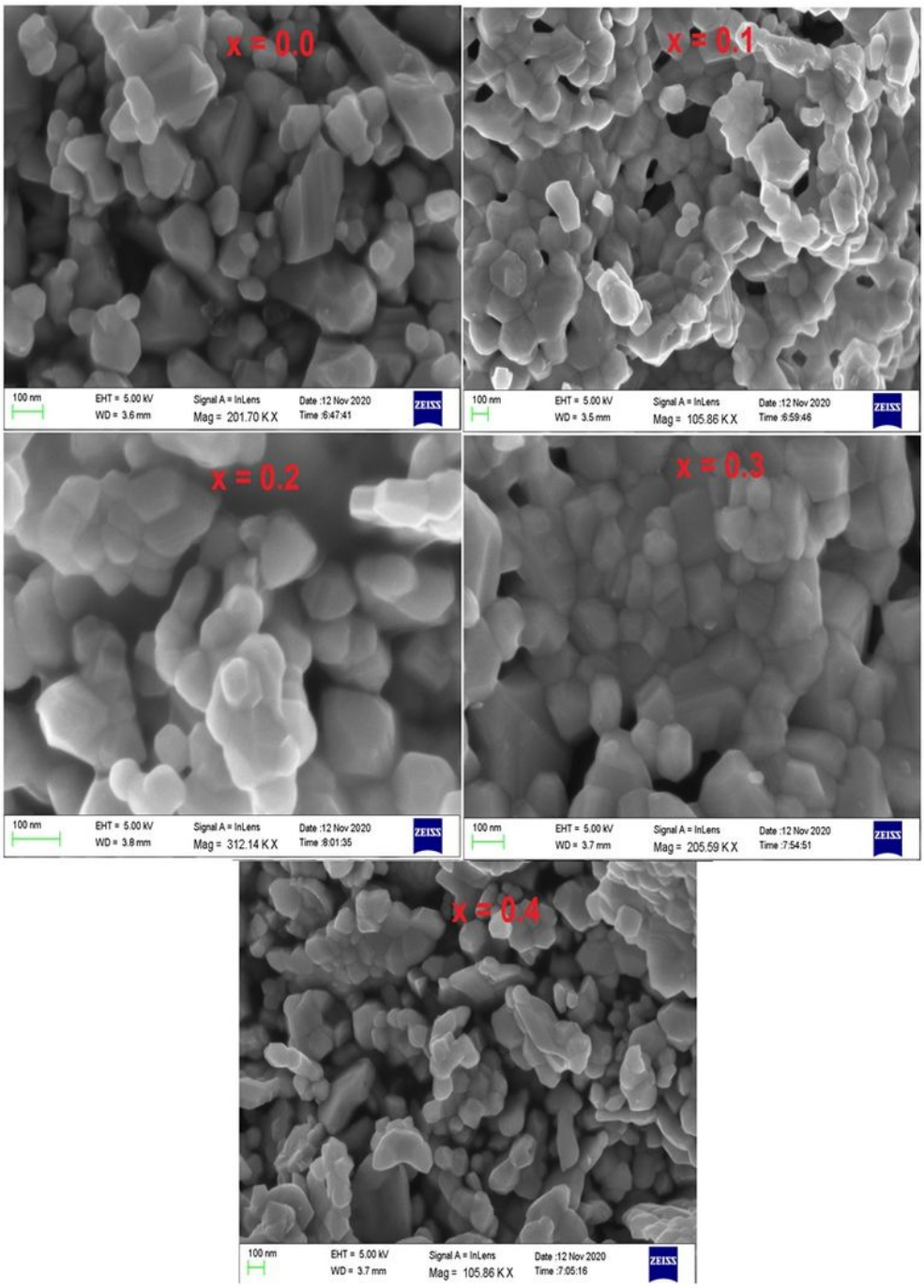

Figure 3

FESEM images for of Ni0.5-xCuxZn0.5Fe2O4 (x = 0.0, 0.05, 0.1, 0.15 and 0.2) ferrites

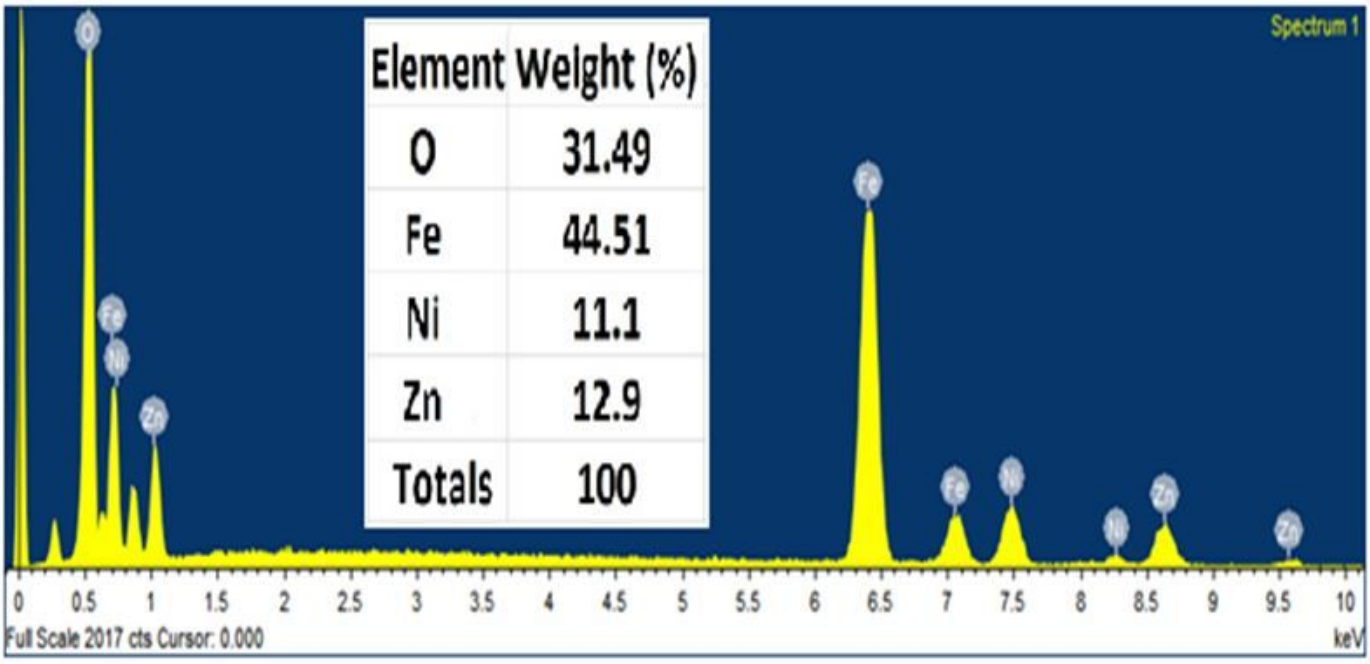

Figure 4

EDS counts and elemental weight for Ni0.5Zn0.5Fe2O4 ferrite NPs

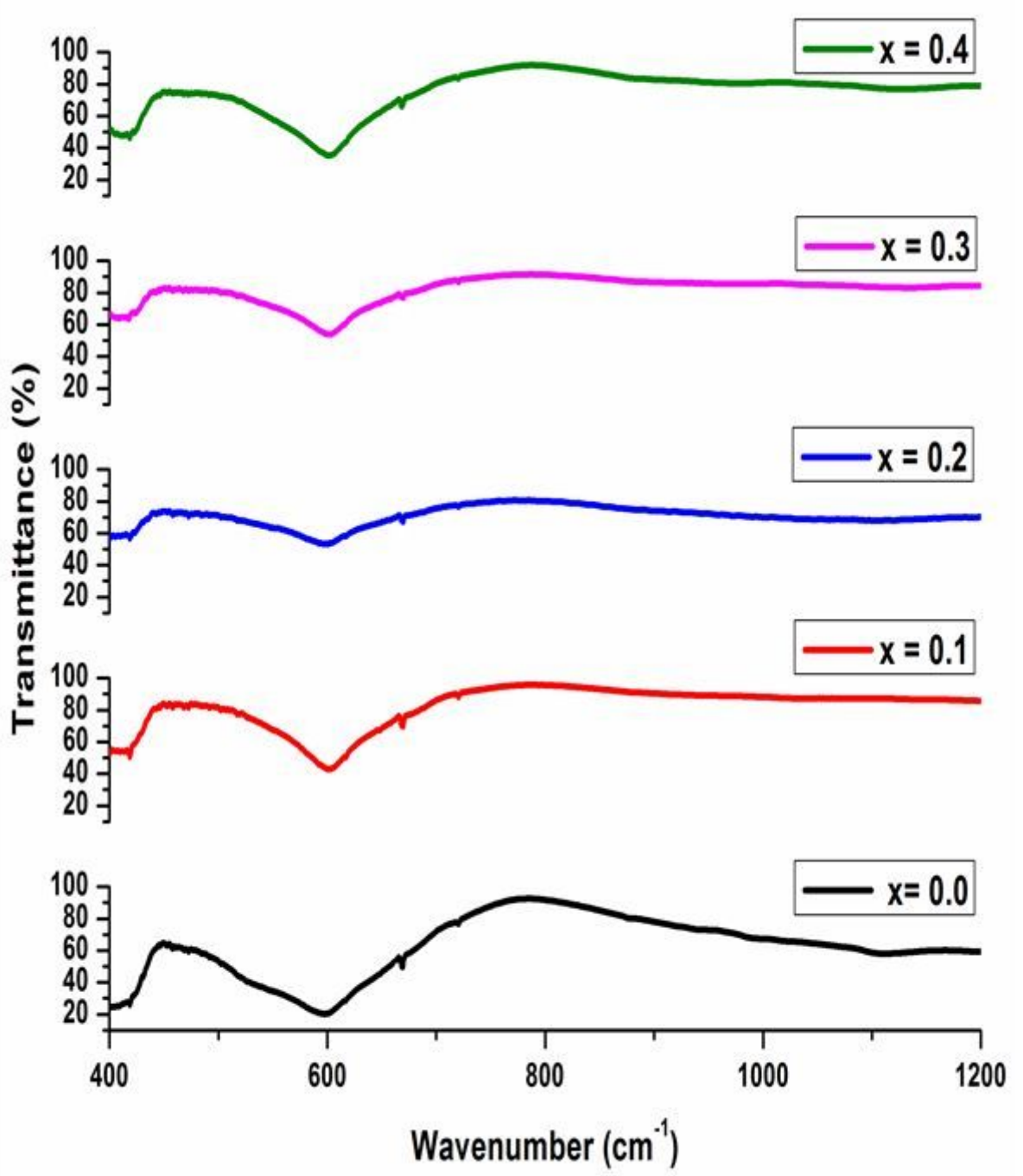

Figure 5

Infrared spectra of of Ni0.5Zn0.5-xCuxFe2O4 (x=0.0, 0.01, 0.2, 0.3 and 0.4) ferrites

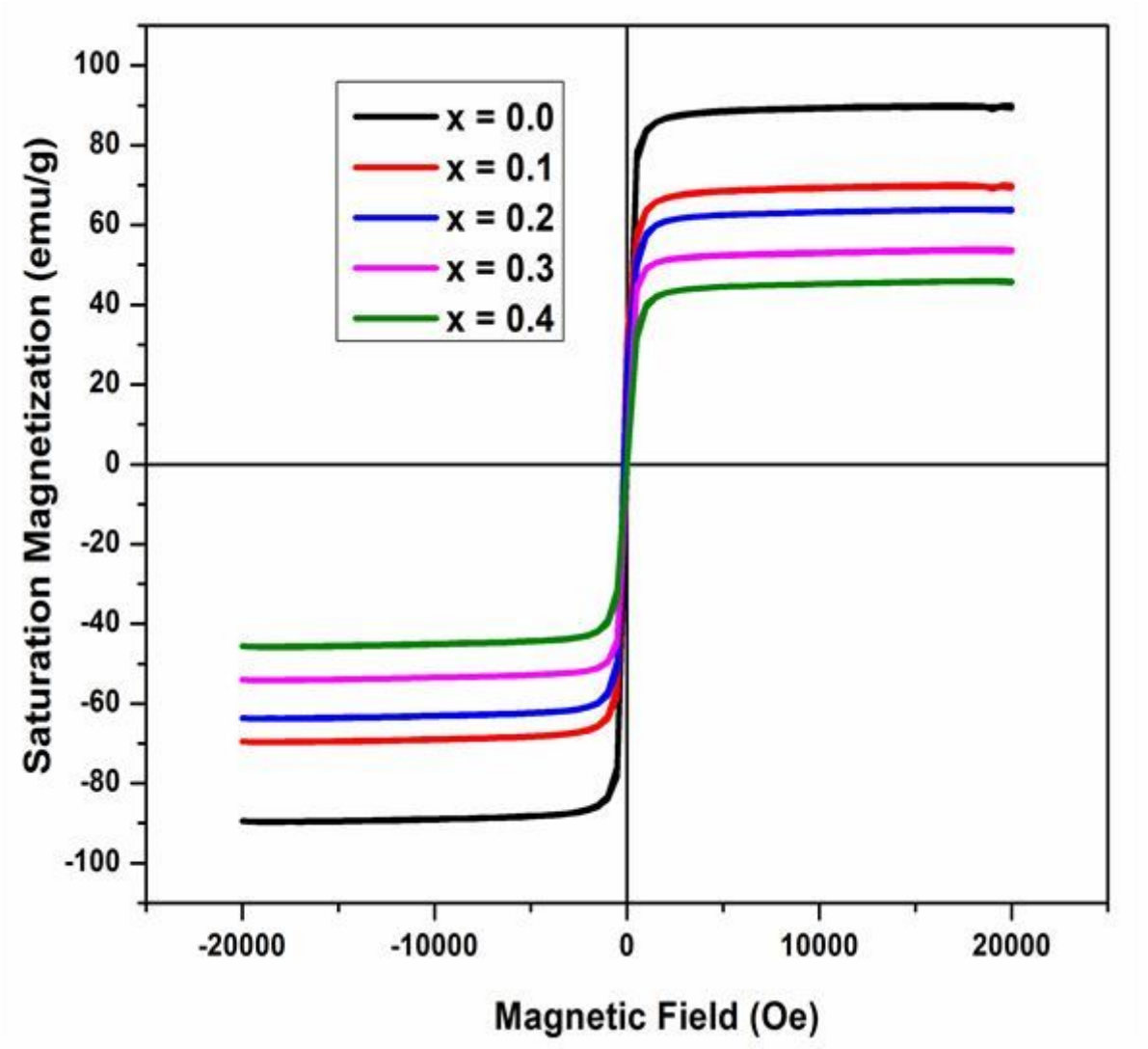

Figure 6

Hysteresis curve of Ni0.5Zn0.5-xCuxFe2O4 (x=0.0, 0.01, 0.2, 0.3 and 0.4) ferrites

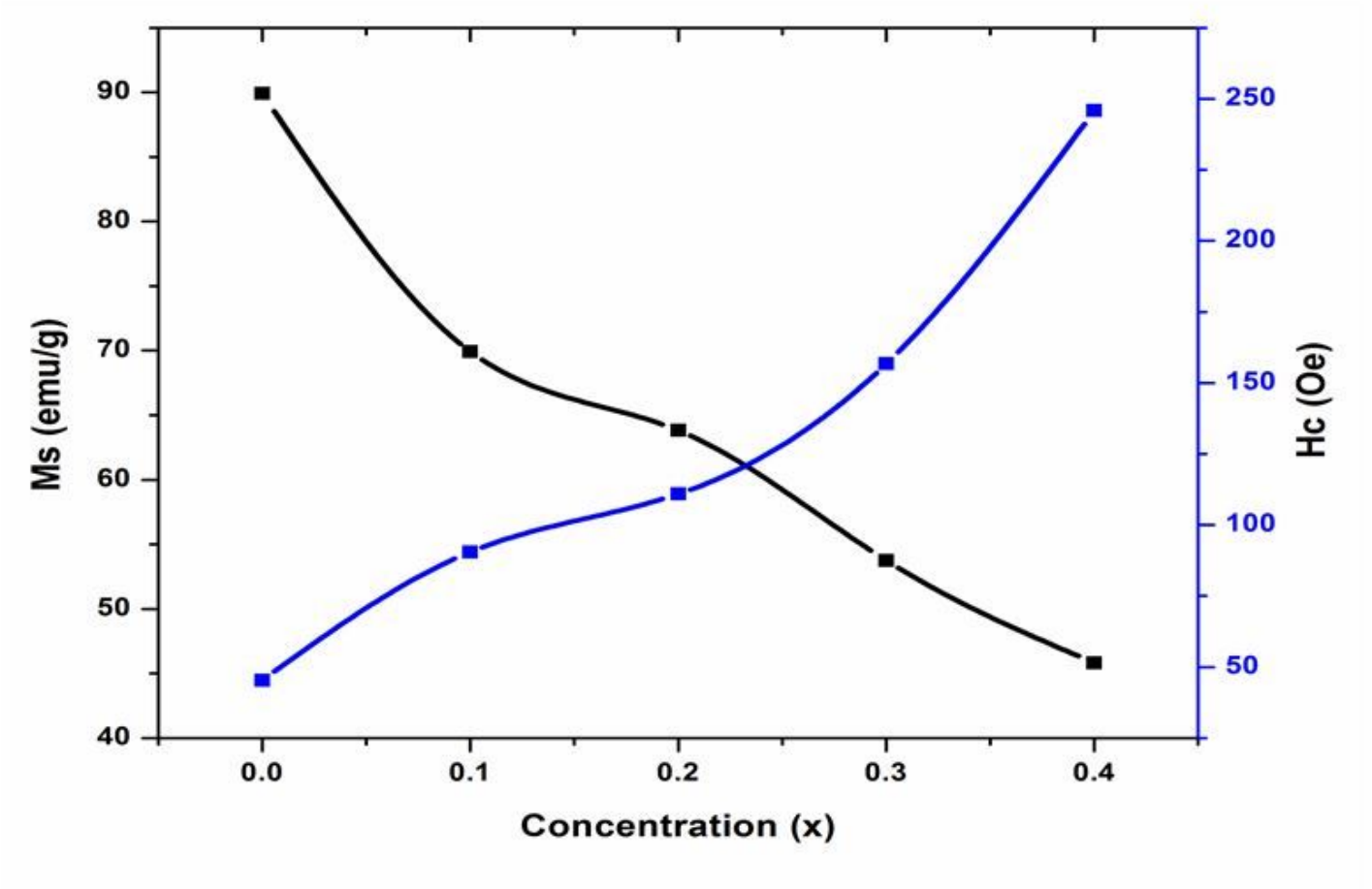

Figure 7

Variation of saturation magnetization and coercivity of Ni0.5Zn0.5-xCuxFe2O4 (x=0.0, 0.01, 0.2, 0.3 and 0.4) ferrites

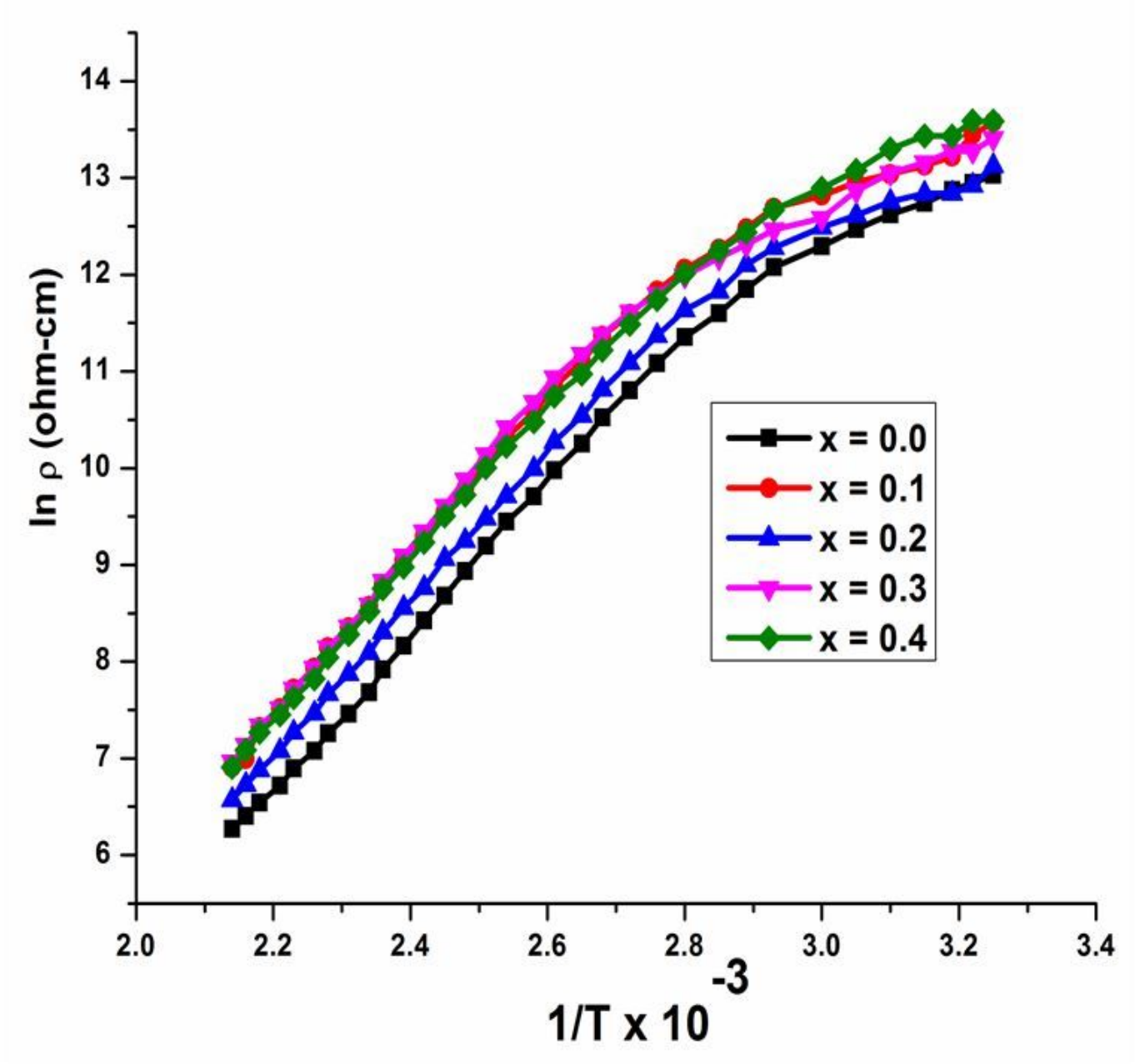

Figure 8

Temperature dependence of DC resistivity of Ni0.5Zn0.5-xCuxFe2O4 (x=0.0, 0.01, 0.2, 0.3 and 0.4) ferrites

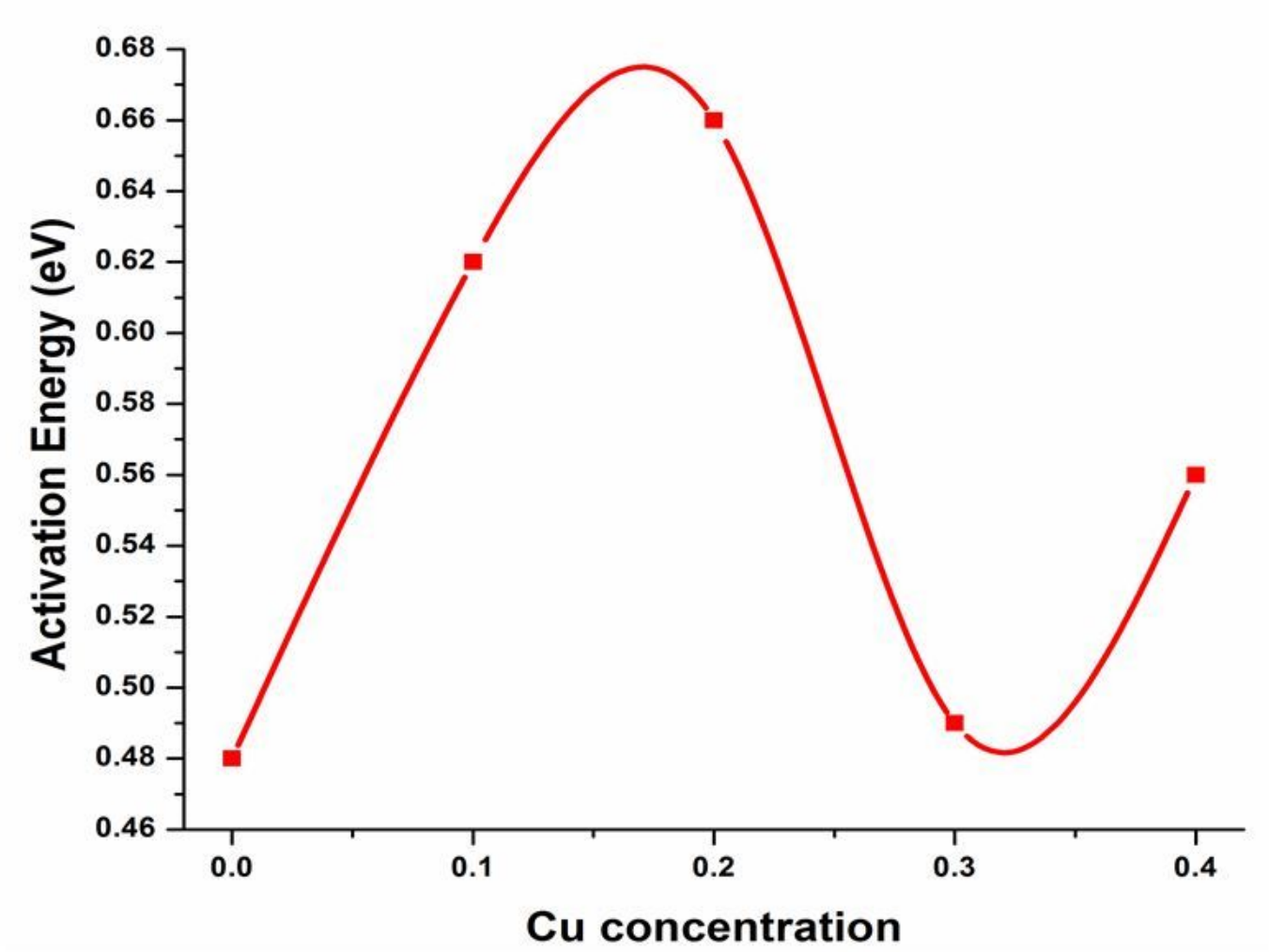

Figure 9

Activation energies of the Ni0.5Zn0.5-xCuxFe2O4 (x=0.0, 0.01, 0.2, 0.3 and 0.4) ferrites